# Viewing Lobate Patterns on Mars and Earth as Climate Modulated Fluid-like Instabilities

**JohnPaul Sleiman[1], Susan J. Conway[3], Andreas Johnsson[4], James Wray[5], Rachel Glade[1,2]**

[1]Department of Earth and Environmental Sciences, University of Rochester, Rochester, NY 14627

[2]Department of Mechanical Engineering, University of Rochester, Rochester, NY 14627

[3]Nantes Université, Univ Angers, Université du Mans, CNRS UMR 6112 Laboratoire de Planétologie et Géosciences, France

[4]Department of Earth Sciences, University of Gothenburg, Box 460, SE-405 30 Gothenburg, Sweden

[5]School of Earth and Atmospheric Sciences, Georgia Institute of Technology, Atlanta, GA, 30332

Corresponding author: JohnPaul Sleiman (jsleiman@ur.rochester.edu)

**This manuscript is a non-peer reviewed preprint that has been submitted to EarthArXiv.**
**The paper has been submitted to ICARUS for peer review.**

# Viewing Lobate Patterns on Mars and Earth as Climate Modulated Fluid-like Instabilities

**JohnPaul Sleiman[1], Susan J. Conway[3], Andreas Johnsson[4], James Wray[5], Rachel Glade[1,2]**

[1]Department of Earth and Environmental Sciences, University of Rochester, Rochester, NY 14627

[2]Department of Mechanical Engineering, University of Rochester, Rochester, NY 14627

[3]Nantes Université, Univ Angers, Université du Mans, CNRS UMR 6112 Laboratoire de Planétologie et Géosciences, France

[4]Department of Earth Sciences, University of Gothenburg, Box 460, SE-405 30 Gothenburg, Sweden

[5]School of Earth and Atmospheric Sciences, Georgia Institute of Technology, Atlanta, GA, 30332

Corresponding author: JohnPaul Sleiman (jsleiman@ur.rochester.edu)

**Abstract**

Lobate features found on high-latitude slopes on Mars resemble terrestrial cold-climate soil patterns known as solifluction lobes. Whether this provides evidence of freeze thaw processes on Mars or pattern equifinality is up for debate. Guided by recently developed theory for solifluction pattern formation inspired by fluid instabilities, here we compare HiRISE imagery of Martian lobes with a large dataset of solifluction lobes on Earth and find that they exhibit similar morphologic scaling. Our data show that Martian lobes are roughly 2.6 times taller than their Earth counterparts, indicative of lobe height set by cohesive soil strength under different gravitational conditions. We also explore possible climate controls on Martian lobe morphology using elevation, aspect, and temperature data. Our work suggests mechanistic similarities between lobate patterns on Earth and Mars that point toward icy origins for these features, with implications for our understanding of climate controls on Martian surface processes.

## 1 Introduction

Modern Mars has a cold, hyper-arid climate, but a key question is how the Martian climate changed during the Late Amazonian (Levy et al., 2009; Gallagher et al., 2011) and whether contemporary liquid water currently exists on Mars (Wray et al., 2021). Geological and geomorphic features may be used to understand surface processes or past climate (MEPAG, 2020; Cronin et al., 1999), and can also lend insight into the underlying mechanics of surface pattern formation in general. Many surface features on Mars have potential Earth counterparts, such as riverbeds (Wray et al., 2021), deltas (Di Achille & Hynek, 2010), drainage networks (e.g., Carr 1995), dunes (Gunn and Jerolmack 2022; Alvarez 2021; Duran Vinent et al., 2019) and in high-latitude regions, lobate patterns (Balme et al., 2013; Gallagher et al., 2011; Gastineau et al., 2020). Here, we use remote sensing imagery to study lobate patterns on Mars (Figure 1) and determine whether they exhibit similar morphologic scaling as solifluction lobes found in cold climates on Earth. We discuss implications for both climate history on Mars and our general understanding of the underlying physics of these enigmatic patterns on both planets.

Several studies have suggested that Mars' high latitudes may have been subjected to freeze-thaw conditions in recent climate history (Gallagher et al., 2011; Balme & Gallagher, 2013; Johnsson et al., 2012). One of the key geomorphic indicators of freeze-thaw action has been small-scale lobes (SSL) (e.g., Gastineau et al., 2020) (Figure 1A,B). Their presence only at high latitudes and similarity in aspect ratio to solifluction lobes (Gastineau et al., 2020) supports the notion that ground ice is required for their formation. However, many open questions remain about these patterns: Why are they significantly larger than their Earth counterparts? Are they quantitatively similar to terrestrial lobes? Are they active or relict (Dundas et al., 2019)?

On Earth, solifluction is defined as the downslope motion of thawed, saturated soil with slow deformation rates of mm-cm/yr (Matsuoka et al., 2001) (Figure 1C,D). It generally occurs in permafrost areas where the active layer experiences frost heave during the winter via the formation of ice lenses (Taber et al., 1930), followed by thawing and saturated flow during the summer (Matsuoka 2001; Harris et al., 1997; Harris et al., 2008). While climate clearly plays a role in their formation (e.g., Lewkowicz, 1992; Larsson, 1982), there is no currently accepted physical model for solifluction, calling into question the absolute necessity for freeze-thaw in both terrestrial and Martian lobes.

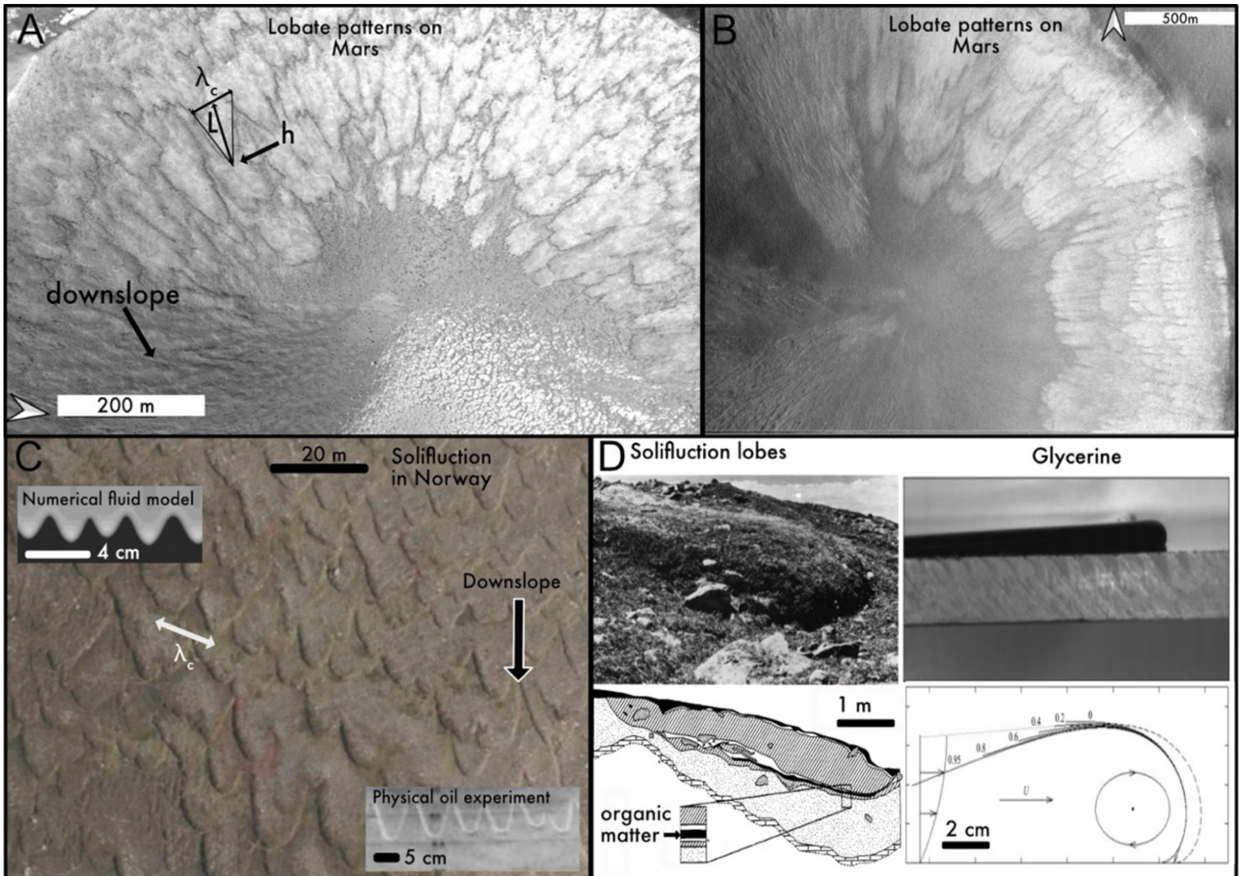


Figure 1: A) Lobate patterns on Mars located in a 4 km-wide crater at 65° N 335° E (HiRISE ESP_025901_2460, patch 7), annotated to show downhill slope direction, lobe width or wavelength $\lambda_c$ , lobe length L, and the location of lobe riser height h measurement. B) Example of larger lobate patterns located in a ~2.4 km-wide crater at 72° N 126° E (ESP_027768_2525, patch 8) C) Orthophoto of solifluction lobes in Norway (The Norwegian Mapping Authority) with overlays of fluid contact line instabilities in a numerical model (upper left; Kondic and Diez 2001) and physical experiment (lower right; Huppert 1982). D) Comparison of solifluction lobes and glycerine flowing down a plane. Upper left: Solifluction lobe in Colorado (Benedict 1970). Lower left: Map of trenched lobe in Norway, with soil organic layer showing rollover motion (Elliott, 1996). Right: Image and schematic of glycerin front also showing rollover motion. Numbers indicate profile evolution through time, and the dashed line illustrates the profile at the next moment. (Veretennikov et al., 1998) Parts C and D modified from Glade et al. (2021).

A recent study (Glade et al., 2021) suggests that solifluction patterns resemble familiar patterns found at fluid flow fronts—known as "contact line instabilities"– seen in everyday phenomena like cake icing or paint streaking down a wall (Huppert 1982) (Figure 1). Such instabilities arise due to the tug-of-war between gravity at a fluid front, which promotes fluid motion, and cohesion, especially surface tension, which restrains the fluids (Troian 1989). Solifluction lobes also have a raised soil front known as a riser (Matsuoka 2001) and may experience similar competition between gravity and soil cohesion. Glade et al. (2021) developed a theoretical scaling relationship that predicts cross-slope lobe wavelength $\lambda_c$ as a function of initial soil thickness $h_0$, topographic slope $\sin\theta$, and an unknown downslope length scale $\gamma$ (Eqn. 1). Using high resolution LiDAR imagery from over 20 sites across Norway, they found that lobe wavelengths generally obey the relation in Eqn. 1, suggesting that solifluction lobes behave similarly to a fluid instability. Acknowledging that solifluction lobes are found only in cold places, Glade et al. (2021) also use historic climate data to show that lobes increase in size at higher elevations and colder temperatures, suggesting that solifluction patterns behave as climate-modulated fluid-like instabilities. However, the exact mechanisms for climate control on solifluction pattern formation remain unknown.

Here we build on the work of Glade et al. (2021) and Gastineau et al. (2020) and use an improved method to measure lobe morphology (wavelength, upslope length, riser height, and slope) on Mars with DTMs (digital terrain models) derived from HiRISE (High Resolution Imaging Science Experiment) imagery (see Methods) and compare to lobe morphology data from a large dataset in Norway. We find that lobate patterns on Mars 1) exhibit similar morphologic scaling to those on Earth and 2) follow the first order theoretical expectation for fluid-like instabilities. This suggests similar formational mechanisms, lending credence to the idea that Martian lobes are formed by similar processes to those that form terrestrial solifluction lobes. We also propose a gravitational scaling that can explain the larger lobe sizes observed on Mars and is supported by our results. Using limited modern climate data, we discuss possible climate controls on lobe morphology on Mars and outline the next steps needed to determine whether freeze-thaw processes are indeed required for lobate pattern formation on both Earth and Mars.

## 2. Materials and Methods

### 2.1 Theoretical Scaling

Here we derive a more generalized version of the scaling analysis done by Glade et al. (2021). We also incorporate gravity, providing an explanation for the difference in lobe size between Mars and Earth. Fingering instabilities at thin film fluid fronts flowing down a plane produce a preferred wavelength that reflects competition between gravity and surface tension such that $\lambda \sim \left(\frac{h_0\sigma}{\rho g \sin\theta}\right)^{1/3}$ (e.g., Huppert 1982; Troian 1989; Kondic and Diez 2001), where $h_0$ is the initial fluid depth, $\sigma$ is the surface tension, $\rho$ is fluid density, $g$ is gravity and $\theta$ is the angle of incline. Inspired by the striking visual similarity between solifluction lobes and contact line instabilities, we develop a simple scaling analysis in an effort to predict cross-slope solifluction lobe wavelengths. This analysis differs from that of a contact line instability in two main ways. First, thick deposits of soil are unlikely to have any form of surface tension due to their granular nature as well as their size; however, soil cohesion may play a similar role. Second, because natural landscapes are inherently bumpy, especially in freeze thaw environments, a hydrostatic pressure term cannot be ignored. Assuming a fluid-like rheology, under hydrostatic conditions for a laminar flow down an inclined plane, the basal shear stress just upstream of the front is $\tau_0 = \rho g h \sin\theta - \rho g h \frac{dh}{dx}$. Because the rheology of slowly creeping icy soil is largely unknown, we avoid assuming a particular rheology and define a bulk viscosity $\mu$ such that $\tau_0 = \mu \frac{U}{h}$, where $U$ is the vertically averaged downhill-directed velocity. Glade et al. (2021) allowed viscosity to vary in the downhill direction in an attempt to account for possible increases of cohesion toward the front as an analogue for surface tension; however, here we relax this assumption and allow for a constant bulk viscosity. Solving the continuity equation at steady state, retaining only first order terms and nondimensionalizing, we find a scaling relationship between cross-slope wavelength $\lambda_c$ and original soil depth $h_0$, topographic slope $\sin(\theta)$, and an unknown downslope length scale $\gamma$ as follows:

$$\lambda_c \sim \sqrt{\frac{h_0\gamma}{\sin(\theta)}} \quad (1)$$

which is identical to the scaling relationship found in Glade et al. (2021) (see Supplementary Materials for full derivation). The physical nature of $\gamma$ is unclear but may be related to soil cohesion or the initial local downslope length of soil in motion that forms a lobate front. Our analysis suggests that accounting for variations in viscosity/cohesion is not necessary for predicting first order scaling. This also supports the idea that knowledge of specific rheology is not vital for a first-order scaling analysis, because only first order terms are retained, as has been shown in contact line instabilities in non-Newtonian fluids (e.g., De Bruyn et al., 2002; Hu and Kieweg, 2015). However, we note that variations in viscosity/cohesion and complex rheology may still be important for the initial onset of the instability (see Discussion).

Note that gravity and viscosity both cancel out in Eqn. 1 ; however, lobate patterns on Mars are larger than those on Earth (Gastineau et al., 2020), suggesting a gravitational control. We propose that gravity enters into the problem by determining $h_0$, the initial soil depth behind the front. Following a simple soil strength argument, a vertical wall of soil characteristic of solifluction risers would be able to build to a certain height dictated by competition between cohesion and gravity (e.g., Abramian et al., 2020):

$$h_0 \sim \frac{C}{\rho g \sin\theta} \quad (2)$$

This would imply that, all other terms held equal, a decrease in gravity should result in lobes with greater height and therefore greater wavelength. The height difference should mimic the inverse of the gravitational difference between the two planets; therefore, we would expect lobe heights to be ~2.64 times larger on Mars than on Earth. Similarly, changes in cohesion should affect the height and subsequent wavelength of the lobes. Thus, even though gravity and cohesion are not explicitly included in Eqn. 1, they influence the initial soil depth h_0 available for motion and the resulting wavelengths.

## 2.2 Remote Sensing

To determine whether Martian lobes exhibit similar morphology to terrestrial solifluction lobes and follow a first-order scaling relationship like that of a fluid instability, we analyzed digital terrain models (DTMs) derived from HiRISE at ~1 m/pixel resolution. This analysis allowed us to measure Martian lobe morphology, including lobe width (wavelength), riser height, and topographic slope, and compare these features with terrestrial lobes. We utilized 7 out of 8 publicly available DTMs from Gastineau et al. (2020), all sourced from the NASA HiRISE archive (Supplemental Materials). One southern hemisphere site from the original study was excluded due to the absence of clearly identifiable lobate patterns. The study involved three main maps from NASA HiRISE: (1) the DTM, projected locally using a sinusoidal projection with a grid spacing of 1 or 2 meters, (2) the Figure of Merit (FOM) map, showing stereo correlation quality for each pixel, and (3) an orthoimage—a visible light image of the location. We used the orthoimage to locate the lobe's front (referred to as the "nose") and its endpoints ("arms"). We then created an aspect-slope map from the DTM at 100-m length scales using the SAGA-GIS Simple Filter with Smooth and Square parameters (radius: 4 or 8 cells depending on grid spacing). This aspect-slope map indicated the steepest slope direction at each lobe nose, reported as angles from 0-360 degrees (0 = North-facing, 90 = East-facing, 180 = South-facing, 270 = West-facing).

For both Martian and terrestrial lobes, an improved method was employed to: (1) automatically determine downslope directions using aspect data, (2) orient measurements of wavelength and lobe length based on the downslope direction, and (3) use a rolling window approach to capture the topographic profiles over distances larger than the lobe itself but small enough to avoid curvature from hillslopes or crater walls. A new script was developed in Python 3 using the Geospatial Data Abstraction Library (GDAL) to improve data quality from the original Glade et al. (2021) method. This code (Supplemental Data) calculates 3D scaling parameters by following these steps: 1) Determine the length of each arm of the lobe based on the (x, y) displacement from the end of the arm to the lobe nose. 2) Calculate the direction of the steepest slope at the nose using the aspect-slope map. 3) Generate a line 180 degrees opposite the steepest slope descent and additional lines aligned with the shortest arm and at a 90-degree offset to the longest arm. 4) Define the slope by finding the lobe's length along the steepest ascent line and doubling this length to extend 0.25 times downhill towards the crater center and 1.75 times uphill. And then 5) Use a “rolling window” approach to determine detrended slope profiles based on specific lobe locations on the DTM.

Riser heights were calculated using detrended topographic profiles aligned with the lobe nose. The tallest local maximum between the lobe front and the top of the lobe was subtracted from the lowest local minimum between the estimated lobe front to account for minor errors in lobe front identification. The window size was lobe length-controlled to avoid skewing by either the crater’s concavity (if too long) or the lobe itself (if too short). Lobe height was defined as the distance from the front to the top of the lobe, using the lobe width as a reference for individual lobes. Heights were then filtered using the FOM map. Lobes with poor DTM accuracy (FOM < 60) were excluded (Supplemental figure 1).

## 3 Results and Discussion

### 3.1 Lobe Morphology

Guided by Eqn. 1, we plot lobe wavelength against lobe riser height divided by topographic slope (Figure 2). Because we do not have constraints on the length scale $\boldsymbol{\gamma}$ in Eqn. 1, we do not attempt to constrain this from remote sensing and do not include it in the plot. Our results show that while Martian lobes are larger on average, they obey a similar scaling relationship to their terrestrial counterparts (Figure 2A). Due to substantial scatter in the data and differences in data quality between Mars and Earth, we use bootstrapping to constrain the most likely power law exponents for each dataset and find that they are indeed similar and center around an exponent of 0.5 (Fig 2B), which matches our theoretical expectations (Eqn. 1). We normalize the morphology data by average wavelength, height, length, and slope for each planet and find that Martian and terrestrial lobes collapse and exhibit similar scatter (Figure 2C), illustrating that the main difference between the two datasets is the larger lobe size on Mars. We note that although a large amount of scatter remains in Figure 2, our new method of lobe measurement significantly decreases the scatter that was observed for terrestrial lobes in Glade et al. (2021). The large scatter is not surprising, due to a lack of constraints on $\gamma$ and other possibly important factors such as cohesion, soil type, and environmental conditions, in addition to error in the remote sensing data and measurement of lobes. Regardless, the clear similarity in scaling between Martian and Earth lobes strongly suggests that they formed due to similar physical mechanisms. Further, the general agreement with the simple scaling prediction from Eqn. 1 furthers the idea that they behave similar to fluid instabilities.

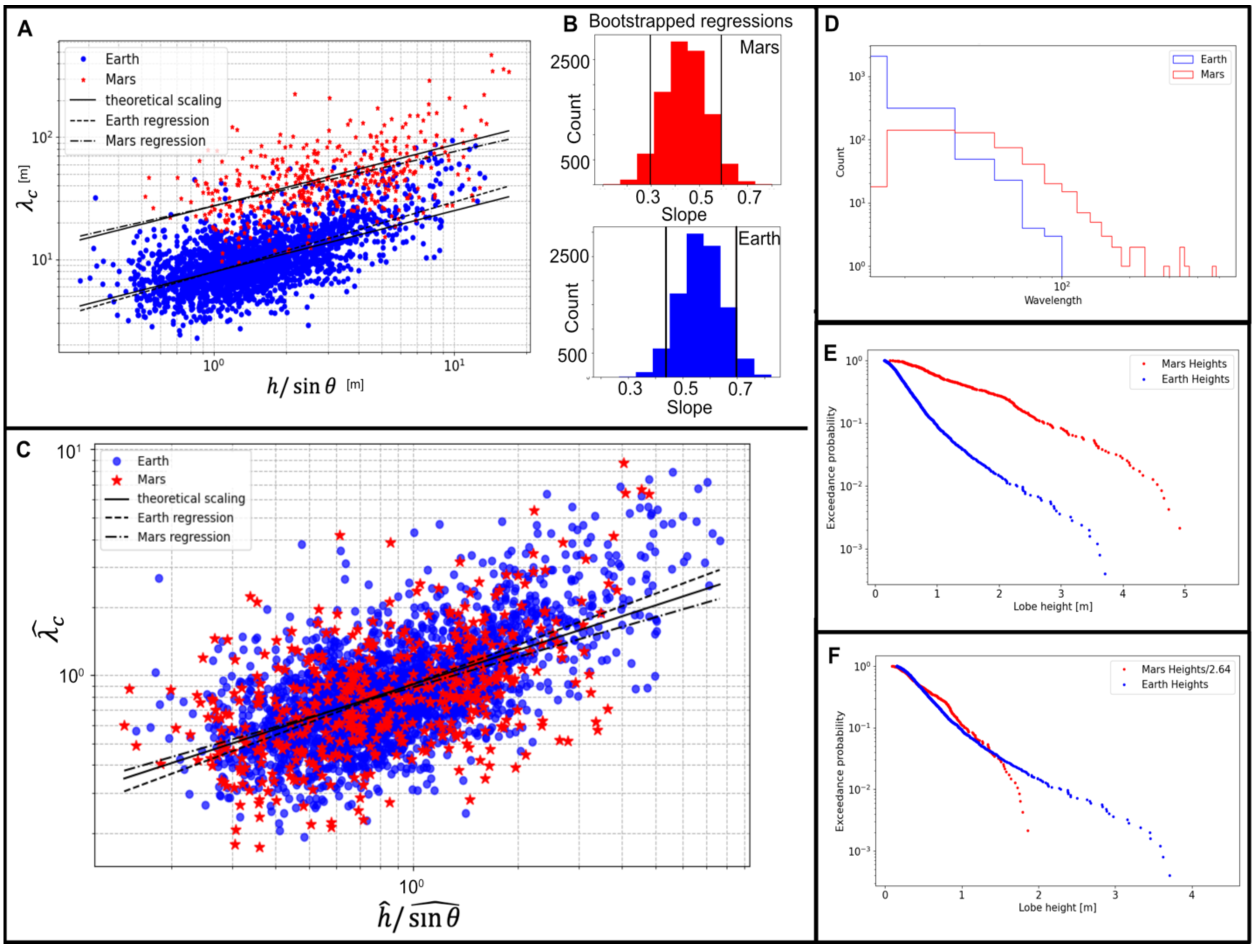


*Figure 2: Comparison of lobe morphology on Mars and Earth. A) Lobe wavelength plotted against height/slope for Mars (red stars) and Earth (blue points). The solid black line shows the theoretical prediction from Eqn. 1, oriented vertically using the best fit intercept from a linear regression of the logged data. The dash-dotted and dashed lines show the best fit line from regression on the logged data for Mars and Earth, respectively. B) Histograms of bootstrapped regression slopes for Mars and Earth with sample size n=100 for 10,000 bootstrapping iterations. C) Normalized plot showing dimensionless lobe wavelength (wavelength normalized by the average wavelength for each planet) plotted against dimensionless lobe height (height normalized by the average lobe height for each planet) divided by slope (slope normalized by the average slope for each planet). D) Histogram of lobe wavelengths E) Exceedance probability plot of lobe height F) Exceedance probability plot of lobe height, where Mars heights are divided by 2.64 (the expected difference in height from Eqn. 2).*

To quantify the difference in lobe size between Mars and Earth, we plot a histogram of lobe wavelength and find that while there is substantial overlap, lobes on Mars exhibit much larger wavelengths (Figure 2D); while the maximum wavelength on Earth is around 100 m, Martian lobes reach wavelength greater than 400 m. The mean wavelengths are 12 m and 54 m on Earth and Mars, respectively. Lobe height also differs between the two planets, with a ratio between the average Mars and Earth heights of 2.6. Because averages are not necessarily meaningful for non-normal distributions, we also plot the exceedance probability of lobe heights on both planets and find that Martian lobes are taller (Figure 2E). To test our prediction that lobe size differs by a factor of 2.64 as expected from soil stability under low gravity conditions (Eqn. 2), we divide the Martian heights by 2.64 and show that the exceedance probability curves lie on top of one another (Figure 2F). We do not expect the tails to overlap due to the small sample size on Mars. This suggests that lower gravity on Mars allows lobes to grow larger, illuminating a key physical mechanism important for lobe morphology.

**3.2 Possible Climate Controls**

How climate controls the formation of these features remains an open question. The fact that lobate patterns are only found in cold regions on Earth and high latitudes on Mars strongly suggests a connection to ground ice for their formation (Johnsson et al., 2012). However, definitive correlations between climate parameters and lobe presence and morphology remain elusive both on Earth and Mars. Glade et al., (2021) found that lobe size increases with elevation, pointing toward a climate control on their morphology, but correlations with mean annual temperature and temperature amplitude were noisy. Though climate data on Mars are limited, we explore possible climate-related controls on lobe morphology in our dataset by looking at elevation and aspect data, in addition to recently acquired global temperatures (Piqueux et al., 2023) (Supplemental data) and depth to ground ice (Piqueux, 2019). We find that both lobe wavelength and height generally decrease with increasing elevation, pointing toward a climate control on lobe morphology (Figure 3A,B) that is curiously the opposite of that seen on Earth (Glade et al., 2021). This, along with the observation that the elevation trend is not simply due to differences in latitude (Supplementary Materials), suggests a pressure sensitivity on Mars rather than a temperature sensitivity that affects the formation of ices at different surface pressures (Lange et al., 2024), supported by the difference in dry adiabatic lapse rate between Mars and Earth. Relationships with temperature data (average maximum and minimum) derived from Mars Climate Sounder observations may point toward larger lobes in colder regions (Figure 3A,B) (Supplemental Materials) (Piqueux et al., 2023) but are less conclusive, and data resolution are not enough to resolve conditions within the craters. While relationships with depth to ground ice are also inconclusive, it is clear that most of the lobate patterns observed on Mars fall within regions that are thought to currently contain ground ice (Figure 3D) (Piqueux et al., 2019). We also find that almost all measured lobes lie on north-facing slopes in interior crater walls (Figure 3C). Nyström and Johnsson (2014) found a similar aspect dependence in which mid latitude lobes (sites used in this study) are found on north facing slopes, while lobes at higher latitudes are found on south-facing slopes. This suggests a solar insolation control on lobe formation, where mid-latitude lobes prefer north-facing slopes for their ability to experience significant snowpack and frost accumulation, as seen in a similar aspect dependence for Martian gullies (Wilson et al., 2021), while higher latitude lobes prefer south-facing slopes to allow for melt and sublimation of the ice. This contrasts with terrestrial lobes, where little aspect dependence is seen

(Supplementary Materials), perhaps because most terrestrial landscapes have an active layer that thaws for at least a portion of the year, in contrast with high latitudes on Mars where ground ice can exist perennially at the surface (Figure 3D).

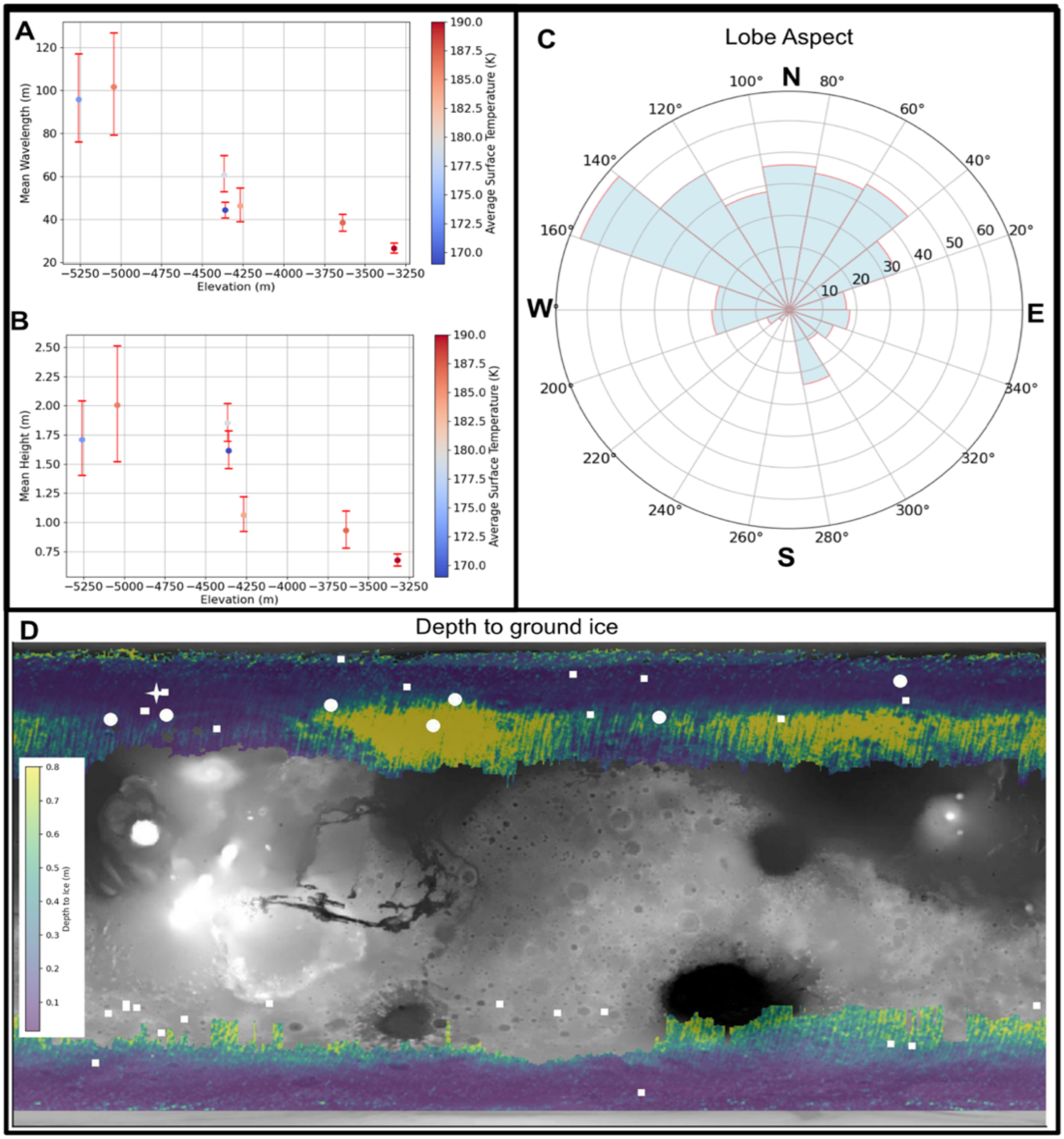


*Figure 3: Exploring possible relationships between lobate patterns and climate on Mars. A,B) Mean lobe wavelength (A) and height (B) for each crater plotted against elevation, with points colored by average surface temperature (Piqueux et al., 2023). Bars indicate 5% and 95% confidence intervals. C) Rose histogram of lobe aspect, illustrating a preference for north-facing slopes D) Base map is a grayscale global elevation data map from Mars Orbiter Laser Altimeter (MOLA) overlain by a depth to ground ice map from Piqueux et al., (2019) then marked with the locations of the DTMs used in this study (white circles), additional stereo pairs from Gastineau et al. (2020) (white squares), and the location of the 2008 NASA Phoenix lander as a point of reference (white star).*

## 5 Conclusions

Our results show that lobate patterns on Mars are quantitatively similar in morphologic scaling to solifluction lobes found in cold regions on Earth. Scaling between lobe wavelength, riser height and topographic slope resembles that expected for a simple fluid-like instability, which is remarkable given the granular nature of these features that operate over exceptionally large length-scales and timescales compared to fluid-like instabilities in paint, for example. Further, the larger size of lobes on Mars can be explained by Mars' lower gravity, which allows lobes to grow approximately 2.6 times larger before they reach their maximum stable height. Thus, our work provides evidence for a simple, fluid-like description of these patterns on both Earth and Mars, and strongly suggests a common formational mechanism for these features. Climate controls on Martian lobe morphology are challenging to characterize given limited data but point toward the idea that lobes favor icy conditions. While our results strongly suggest a common underlying physical framework for lobate patterns on Mars and Earth that resembles that of a climate-modulated fluid instability, current data cannot conclude the necessity of thawed liquid water. For example, it is possible that frost heave and subsequent sublimation of $CO_2$ or other forms of ice can produce these features (Sizemore et al., 2015). We also emphasize that while our theory predicts the scaling of lobate features, it does not predict the conditions necessary for their initial formation. It is likely that a combination of frost heave and soil cohesion results in a unique rheology that allows for the onset of the instability, possibly akin to that of rheology-induced noninertial instabilities seen in shear thickening suspensions (Texier et al., 2020). Future work could establish a better understanding of the physical properties of Martian regolith, including cohesion that may result from clay-sized grains and/or the presence of salts (Sullivan et al., 2011). Laboratory experiments could explore the role of cohesion and rheology in these instabilities, determining whether ice and liquid water are both required for their formation.

**Acknowledgments**

We would like to thank the JMARS and HiRISE teams for troubleshooting help with the Mars DTMS and we would also like to thank David Cúñez and Carson Horne with troubleshooting efforts on the python script.

**Open Research**

All of the map layers, python scripts and data sets is publicly available using a Fig Share repository and can be found in the supplementary materials. https://figshare.com/s/ef41784caadba090a80e

**References**

**Abramian, A., Lagrée, P. Y., & Staron, L. (2021).** How cohesion controls the roughness of a granular deposit. Soft Matter, 17(47), 10723-10729.

**Alvarez, C. A., Cúñez, F. D., & Franklin, E. M. (2021).** Growth of barchan dunes of bidispersed granular mixtures. Physics of Fluids, 33(5).

**Balme, M. R., Gallagher, C. J., & Hauber, E. (2013).** Morphological evidence for geologically young thaw of ice on Mars: A review of recent studies using high-resolution imaging data. Progress in Physical Geography, 37(3), 289-324.

**Benedict, J. B. (1970).** Downslope soil movement in a Colorado alpine region: Rates, processes, and climatic significance. Arctic and Alpine Research, 2(3), 165-226.

**Carr, M. H. (1995).** The Martian drainage system and the origin of valley networks and fretted channels. Journal of Geophysical Research: Planets, 100(E4), 7479-7507.

**Cronin, T. M. (1999).** Principles of Paleoclimatology. Columbia University Press.

**De Bruyn, J. R., Habdas, P., & Kim, S. (2002).** Fingering instability of a sheet of yield-stress fluid. Physical Review E, 66(3), 031504.

**Di Achille, G., & Hynek, B. M. (2010).** Ancient ocean on Mars supported by global distribution of deltas and valleys. Nature Geoscience, 3(7), 459-463.

**Dundas, C. M., Mellon, M. T., Conway, S. J., & Gastineau, R. (2019).** Active boulder movement at high Martian latitudes. Geophysical Research Letters, 46(10), 5075-5082.

**Duran Vinent, O., Andreotti, B., Claudin, P., & Winter, C. (2019).** A unified model of ripples and dunes in water and planetary environments. Nature Geoscience, 12(5), 345-350.

**Elliott, G. (1996).** Microfabric evidence for podzolic soil inversion by solifluction processes. Earth Surface Processes and Landforms, 21(5), 467-476.

**Farley, K. A., Malespin, C., Mahaffy, P., Grotzinger, J. P., Vasconcelos, P. M., Milliken, R. E., ... & Ramos, M. (2014).** In situ radiometric and exposure age dating of the Martian surface. Science, 343(6169), 1247166.

**Gallagher, C., Balme, M., Conway, S., & Grindrod, P. M. (2011).** Sorted clastic stripes, lobes and associated gullies in high-latitude craters on Mars: Landforms indicative of very recent, polycyclic ground-ice thaw and liquid flows. Icarus, 211(1), 458-471.

**Gastineau, R., Conway, S. J., Johnsson, A., Eichel, J., Mangold, N., Grindrod, P. M., & Izquierdo, T. (2020).** Small-scale lobate hillslope features on Mars: A comparative 3D morphological study with terrestrial solifluction lobes and zebra stripe lobes. Icarus, 342, 113606.

**Glade, R. C., Fratkin, M. M., Pouragha, M., Seiphoori, A., & Rowland, J. C. (2021).** Arctic soil patterns analogous to fluid instabilities. Proceedings of the National Academy of Sciences, 118(21), e2101255118.

**Gunn, A., & Jerolmack, D. J. (2022).** Conditions for aeolian transport in the solar system. Nature Astronomy, 6(8), 923-929.

**Harris, C., Kern-Luetschg, M., Murton, J., Font, M., Davies, M., & Smith, F. (2008).** Solifluction processes on permafrost and non-permafrost slopes: Results of a large-scale laboratory simulation. Permafrost and Periglacial Processes, 19(4), 359-378.

**Hu, B., & Kieweg, S. L. (2015).** Contact line instability of gravity-driven flow of power-law fluids. Journal of non-Newtonian fluid mechanics, 225, 62-69.

**Huppert, H. E. (1982).** Flow and instability of a viscous current down a slope. Nature, 300(5891), 427-429.

**Johnsson, A., Reiss, D., Hauber, E., Zanetti, M., Hiesinger, H., Johansson, L., & Olvmo, M. (2012).** Periglacial mass-wasting landforms on Mars suggestive of transient liquid water in the recent past: Insights from solifluction lobes on Svalbard. Icarus, 218(1), 489-505.

**Kondic, L., & Diez, J. (2001).** Pattern formation in the flow of thin films down an incline: Constant flux configuration. Physics of Fluids, 13, 3168-3184.

**Lange, L., Piqueux, S., Edwards, C. S., Forget, F., Naar, J., Vos, E., & Szantai, A. (2024).** Observations of Water Frost on Mars with THEMIS: Application to the Presence of Brines and the Stability of (Sub) Surface Water Ice. arXiv preprint arXiv:2405.08713.

**Larsson, S. (1982).** Geomorphological effects on the slopes of Longyear Valley, Spitsbergen, after a heavy rainstorm in July 1972. Geografiska Annaler: Series A, Physical Geography, 64(3-4), 105-125.

**Levy, J., Head, J., & Marchant, D. (2009).** Thermal contraction crack polygons on Mars: Classification, distribution, and climate implications from HiRISE observations. Journal of Geophysical Research: Planets, 114(E1).

**Lewkowicz, A. G. (1992).** A solifluction meter for permafrost sites. Permafrost and Periglacial Processes, 3(1), 11-18.

**Matsuoka, N. (2001).** Solifluction rates, processes and landforms: A global review. Earth-Science Reviews, 55(1-2), 107-134.

**MEPAG (2020).** Mars Scientific Goals, Objectives, Investigations, and Priorities: 2020. D. Banfield (Ed.), 89 p. white paper posted March 2020 by the Mars Exploration Program Analysis Group (MEPAG).

**Nyström, E., & Johnsson, A. (2014, April).** Aspect dependence of small-scale lobes in the northern hemisphere of Mars. In European Planetary Science Congress (Vol. 9, pp. EPSC2014-480).

**Piqueux, S., Buz, J., Edwards, C. S., Bandfield, J. L., Kleinböhl, A., Kass, D. M., ... & Heavens, N. (2023).** Mars thermal inertia and surface temperatures by the Mars Climate Sounder. Icarus, 115851.

**Piqueux, S., Kass, D. M., Kleinböhl, A., Slipski, M., Hayne, P. O., McCleese, D. J., ... & Heavens, N. (2019).** Widespread shallow water ice on Mars at high latitudes and midlatitudes. Geophysical Research Letters, 46(24), 14290-14298.

**Sizemore, H. G., Zent, A. P., & Rempel, A. W. (2015**). Initiation and growth of Martian ice l enses. Icarus, 251, 191-210.

**Sullivan, R., Anderson, R., Biesiadecki, J., Bond, T., & Stewart, H. (2011).** Cohesions, friction angles, and other physical properties of Martian regolith from Mars Exploration Rover wheel trenches and wheel scuffs. Journal of Geophysical Research: Planets, 116(E2).

**Taber, S. (1930).** The mechanics of frost heaving. The Journal of Geology, 38(4), 303-317.

**Darbois Texier, B., Lhuissier, H., Forterre, Y., & Metzger, B. (2020).** Surface-wave instability without inertia in shear-thickening suspensions. Communications Physics, 3(1), 232.

**Troian, S., Herbolzheimer, E., Safran, S., & Joanny, J. (1989).** Fingering instabilities of driven spreading films. Europhysics Letters, 10(1), 25.

**Veretennikov, I., Indeikina, A., & Chang, H. C. (1998).** Front dynamics and fingering of a driven contact line. Journal of Fluid Mechanics, 373, 81-110.

**Wilson, S. A., Morgan, A. M., Howard, A. D., & Grant, J. A. (2021).** The global distribution of craters with alluvial fans and deltas on Mars. Geophysical Research Letters, 48(4), e2020GL091653.

**Wray, J. J. (2021).** Contemporary liquid water on Mars? Annual Review of Earth and Planetary Sciences, 49, 141-171.

# Supplemental Material for Viewing Lobate Patterns on Mars and Earth as Climate Modulated Fluid Like Instabilities

This document contains the supplemental scaling analysis and figures from "Viewing Lobate Patterns on Mars and Earth as Climate-Modulated Fluid-Like Instabilities" (Sleiman et al.,).

There are three sections in this document 1) Table outlining metadata related to our site locations with links to find the public data. 2) The full derivation of the theoretical scaling analysis. 3) Supplemental figures of relevance.

**The code that produced the datasets along with figures used in the main manuscipt and supplemental can be found here: link to code and datasets found on figshare.**

## Patch Data

HiRise (High Resolution Imaging Science Experiment) has the three public maps used in this study available on their website. The link to each DTM, FOM and Ortho map is shown below and grouped my patch.

| Location | DTM name | Link | Vertical precision (m) | Latitude (°) | Longitude (°E) |
|---|---|---|---|---|---|
| Patch 2 | ESP_025888_2365 | ESP_025888_2365 | 0.13 | 56.401 | 327.271 |
| Patch 3 | ESP_026314_2390 | ESP_026314_2390 | 0.17 | 58.66 | 217.244 |
| Patch 4 | ESP_019147_2395 | ESP_019147_2395 | 0.38 | 59.4 | 44.4 |
| Patch 5 | ESP_027065_2405 | ESP_027065_2405 | 0.22 | 60.202 | 236.27 |
| Patch 6 | PSP_007429_2440 | PSP_007429_2440 | 0.35 | 63.78 | 292.32 |
| Patch 7 | ESP_025901_2460 | ESP_025901_2460 | 0.16 | 65.768 | 334.797 |
| Patch 8 | ESP_027860_2525 | ESP_027860_2525 | 0.12 | 72.442 | 126.455 |

Table 1: DTM information and links

## Scaling analysis

### 1 Definition of $U$ and $V$

Glade 2021 starts with defining the basal shear stress as hydrostatic conditions for a laminar fluid going downslope, where $\rho$ is the bulk density, $g$ is gravity, $h$ is the fluid depth at the front, and $\theta$ is the underlying slope:

$$\tau_{(0x)} = \rho g h \sin(\theta) - \rho g h \frac{\partial h}{\partial x} \tag{1}$$

Next we have to assume it has a newtonian rheology without a particular power law, with an average velocity across the colum $\mu$, the bulk viscosity can de defined as (in the downhill x direction):

$$\tau = \mu \frac{U}{h} \tag{2}$$

Combining the equations, and rearranging to find U (which is the vertically averaged velocity in the x direction) we get:

$$-\mu\frac{U}{h} = -\rho gh\sin(\theta) + \rho gh\frac{\partial h}{\partial x} \tag{3}$$

$$U = \frac{\rho gh^2\sin(\theta)}{\mu} - \frac{\rho gh^2\frac{\partial h}{\partial x}}{\mu} \tag{4}$$

and we find V (which is the averaged velocity in the y direction):

$$V = \frac{-\rho gh^2}{\mu}\frac{\partial h}{\partial y} \tag{5}$$

## 2 Continuum

Continuum states (assuming steady state):

$$\frac{\partial h}{\partial t} = \frac{\partial(q_x)}{\partial x} + \frac{\partial(q_y)}{\partial y} \tag{6}$$

$$\frac{\partial h}{\partial t} = 0 = \frac{\partial(q_x)}{\partial x} + \frac{\partial(q_y)}{\partial y} \tag{7}$$

where $q_x = hU$, $q_y = hV$, coming from the hydrostatic pressure gradient:

**2a) $Q_x$ term:**

Given that $q_x = hU$:

$$q_x = h\left(\frac{\rho gh^2\sin\theta}{\mu} - \frac{\rho gh^2}{\mu}\frac{\partial h}{\partial x}\right) = \frac{\rho gh^3\sin\theta}{\mu} - \frac{\rho gh^3}{\mu}\frac{\partial h}{\partial x} \tag{8}$$

Differentiating $q_x$ with respect to $x$:

$$\frac{\partial q_x}{\partial x} = \frac{\partial}{\partial x}\left(\frac{\rho gh^3\sin\theta}{\mu} - \frac{\rho gh^3}{\mu}\frac{\partial h}{\partial x}\right) \tag{9}$$

Using the product rule (since $\rho$, $\mu$ and g stay constant they can be removed from the derivative):

$$\frac{\partial q_x}{\partial x} = \frac{\rho g}{\mu}\left(\frac{\partial(h^3\sin\theta)}{\partial x} - \frac{\partial(h^3\frac{\partial h}{\partial x})}{\partial x}\right) \tag{10}$$

Computing $\frac{\partial(h^3\sin\theta)}{\partial x}$:

$$\frac{\partial(h^3\sin\theta)}{\partial x} = 3h^2\sin\theta\frac{\partial h}{\partial x} \tag{11}$$

And computing $\frac{\partial(h^3 \frac{\partial h}{\partial x})}{\partial x}$:

$$\frac{\partial(h^3 \frac{\partial h}{\partial x})}{\partial x} = \frac{\partial h^3}{\partial x}\frac{\partial h}{\partial x} + h^3 \frac{\partial^2 h}{\partial x^2} = 3h^2 \frac{\partial h}{\partial x}\frac{\partial h}{\partial x} + h^3 \frac{\partial^2 h}{\partial x^2} \quad (12)$$

Substituting back in:

$$\frac{\partial q_x}{\partial x} = \frac{\rho g}{\mu}\left(3h^2 \sin\theta \frac{\partial h}{\partial x} - 3h^2 \sin\theta \left(\frac{\partial h}{\partial x}\right)^2 - h^3 \frac{\partial^2 h}{\partial x^2}\right) \quad (13)$$

Simplifying:

$$\frac{\partial q_x}{\partial x} = \frac{3\rho g h^2 \sin\theta}{\mu}\frac{\partial h}{\partial x} - \frac{3\rho g h^2}{\mu}\left(\frac{\partial h}{\partial x}\right)^2 - \frac{\rho g h^3}{\mu}\frac{\partial^2 h}{\partial x^2} \quad (14)$$

**2b) $Q_y$ term:**

Given that $q_y = hV$:

$$q_y = h\left(\frac{-\rho g h^2}{\mu}\frac{\partial h}{\partial y}\right) = \frac{-\rho g h^3}{\mu}\frac{\partial h}{\partial y} \quad (15)$$

Differentiating $q_y$ with respect to $y$:

$$\frac{\partial q_y}{\partial y} = \frac{\partial}{\partial y}\left(\frac{-\rho g h^3}{\mu}\frac{\partial h}{\partial y}\right) \quad (16)$$

Using the product rule (since $\rho$, $\mu$ and g stay constant they can be removed from the derivative):

$$\frac{\partial q_y}{\partial y} = \frac{-\rho g}{\mu}\left(\frac{\partial(h^3)}{\partial y}\frac{\partial h}{\partial y} + h^3 \frac{\partial^2 h}{\partial y^2}\right) \quad (17)$$

Computing $\frac{\partial(h^3)}{\partial y}$:

$$\frac{\partial(h^3)}{\partial y} = 3h^2 \frac{\partial h}{\partial y} \quad (18)$$

Substituting back in:

$$\frac{\partial q_y}{\partial y} = \frac{-\rho g}{\mu}\left(3h^2 \left(\frac{\partial h}{\partial y}\right)\frac{\partial h}{\partial y} + h^3 \frac{\partial^2 h}{\partial y^2}\right) \quad (19)$$

Simplifying:

$$\frac{\partial q_y}{\partial y} = -\frac{3\rho g h^2}{\mu}\left(\frac{\partial h}{\partial y}\right)^2 - \frac{\rho g h^3}{\mu}\frac{\partial^2 h}{\partial y^2} \quad (20)$$

**2c) Combining $Q_x$ and $Q_y$ term:**

Now remember that $\frac{\partial h}{\partial t} = 0 = \frac{\partial(Qx)}{\partial x} + \frac{\partial(Qy)}{\partial y}$ so let's rearrange.

$$\frac{\partial h}{\partial t} = 0 = \frac{3\rho g h^2 \sin\theta}{\mu}\frac{\partial h}{\partial x} - \frac{3\rho g h^2}{\mu}\left(\frac{\partial h}{\partial x}\right)^2 - \frac{\rho g h^3}{\mu}\frac{\partial^2 h}{\partial x^2} - \frac{3\rho g h^2}{\mu}\left(\frac{\partial h}{\partial y}\right)^2 - \frac{\rho g h^3}{\mu}\frac{\partial^2 h}{\partial y^2} \quad (21)$$

Simplifying we get

$$0 = 3\sin\theta\frac{\partial h}{\partial x} - 3\left(\frac{\partial h}{\partial x}\right)^2 - h\frac{\partial^2 h}{\partial x^2} - 3\left(\frac{\partial h}{\partial y}\right)^2 - h\frac{\partial^2 h}{\partial y^2} \quad (22)$$

We can simplify since all of this equals zero. We can also retain only first order since we assume dh/dx«1.

$$0 = 3\sin\theta\frac{\partial h}{\partial x} - h\frac{\partial^2 h}{\partial x^2} - h\frac{\partial^2 h}{\partial y^2} \quad (23)$$

## 3 Nondimensionalization

Now to non-dimensionalize, we define the variables as:

$$h = H\hat{h} \quad (24)$$

$$x = \gamma\hat{x} \quad (25)$$

$$y = \lambda\hat{y} \quad (26)$$

First, compute the derivatives in terms of the new variables:

$$\frac{\partial h}{\partial x} = \frac{\partial(H\hat{h})}{\partial(\gamma\hat{x})} = \frac{H}{\gamma}\frac{\partial\hat{h}}{\partial\hat{x}} \quad (27)$$

$$\frac{\partial^2 h}{\partial x^2} = \frac{\partial}{\partial x}\left(\frac{H}{\gamma}\frac{\partial\hat{h}}{\partial\hat{x}}\right) = \frac{H}{\gamma^2}\frac{\partial^2\hat{h}}{\partial\hat{x}^2} \quad (28)$$

$$\frac{\partial^2 h}{\partial y^2} = \frac{\partial}{\partial y}\left(\frac{H}{\lambda}\frac{\partial\hat{h}}{\partial\hat{y}}\right) = \frac{H}{\lambda^2}\frac{\partial^2\hat{h}}{\partial\hat{y}^2} \quad (29)$$

Substituting these into equation 28:

$$0 = \frac{3\sin(\theta)H}{\gamma}\frac{\partial\hat{h}}{\partial\hat{x}} - \frac{H^2}{\gamma^2}\frac{\partial^2\hat{h}}{\partial\hat{x}^2} - \frac{H^2}{\lambda^2}\frac{\partial^2\hat{h}}{\partial\hat{y}^2} \quad (30)$$

Retaining only the dimensional leading coefficients:

$$0 = \frac{3\sin(\theta)H}{\gamma} - \frac{H^2}{\gamma^2} - \frac{H^2}{\lambda^2} \tag{31}$$

Simplify:

$$0 = \frac{3\sin(\theta)}{\gamma} - \frac{H}{\gamma^2} - \frac{H}{\lambda^2} \tag{32}$$

Before we see how these terms are related to wavelength, $\gamma$, we must first assume that wavelength we are finding is the cross-slope wavelength. Assuming this means the body force enters at lowest order, $\frac{2\sin\theta}{\gamma}$, we find can drop the other terms and rearrange we find:

$$\lambda \sim \sqrt{\frac{H\gamma}{3\sin(\theta)}} \tag{33}$$

# Supplemental Figures

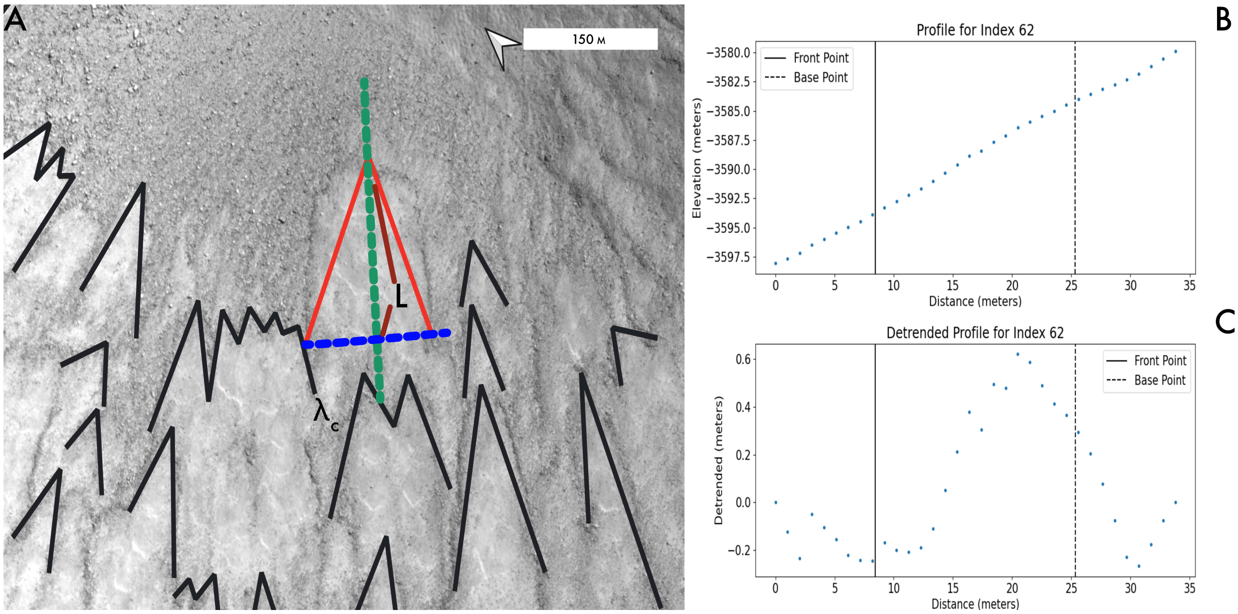


Figure 1: Methods for measuring lobe morphology. A) Black lines indicate triangles drawn in a 2.4 km crater at 72°N 126°E (ESP 027768 2525, patch 7) in QGIS to roughly outline lobes. Centered onto one lobe (outlined in red) the slope line (dashed green) is used for detrending the area around the lobe, the total length of the slope line is based on the length of the lobe (marked by L), which is the front point to the wavelength (outlined in blue) intercept (see methods). B) Elevation profile of an example lobe (lobe 62), with each point representing one pixel. C) Detrended elevation profile of an example lobe (lobe 62), calculated by removing average slope from profile in B and used to calculate lobe height. In B) and C) the solid line indicates the position of the lobe riser taken from the hand-drawn triangles and dashed line indicates the position of the lobe top calculated based on the length of the lobe (correlated to the intercept of the wavelength and the length of the lobe shown in panel A.

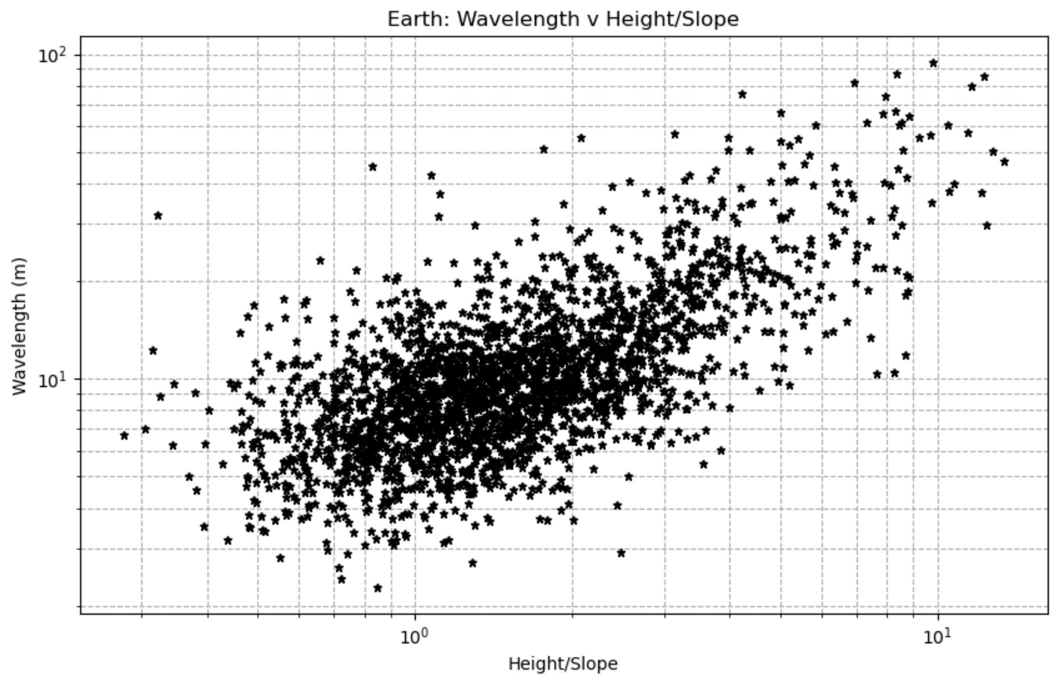


Figure 2: Lobe wavelength plotted against height/slope in log-log space for just the Earth dataset.

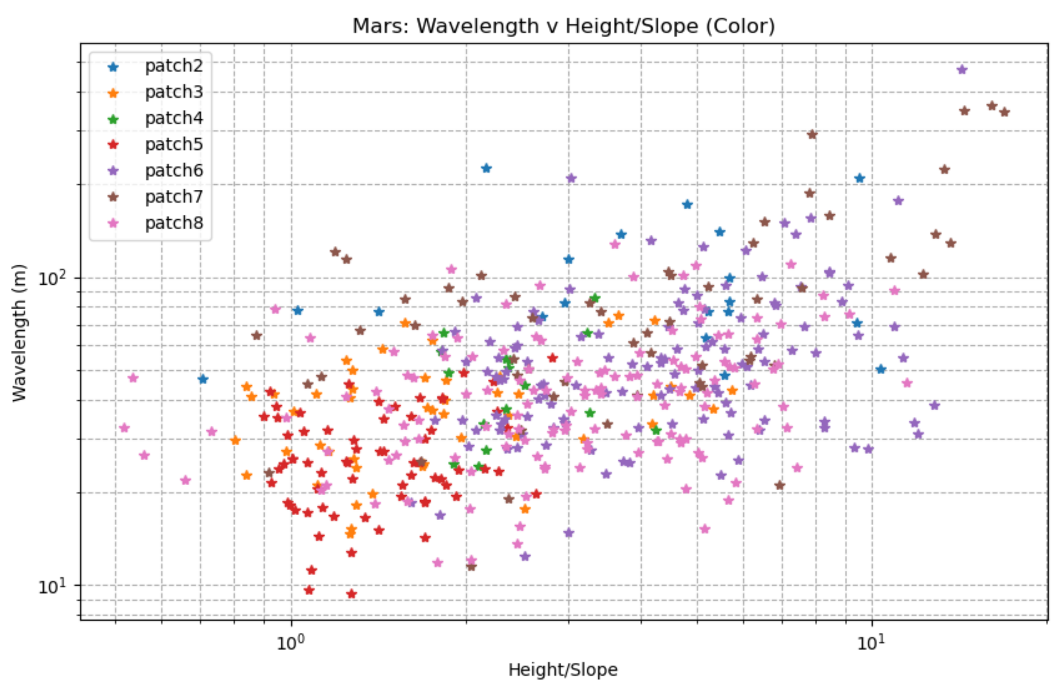


Figure 3: Lobe wavelength plotted against height/slope in log-log space for just the Mars dataset. Colored by the different patch location (different crater location)

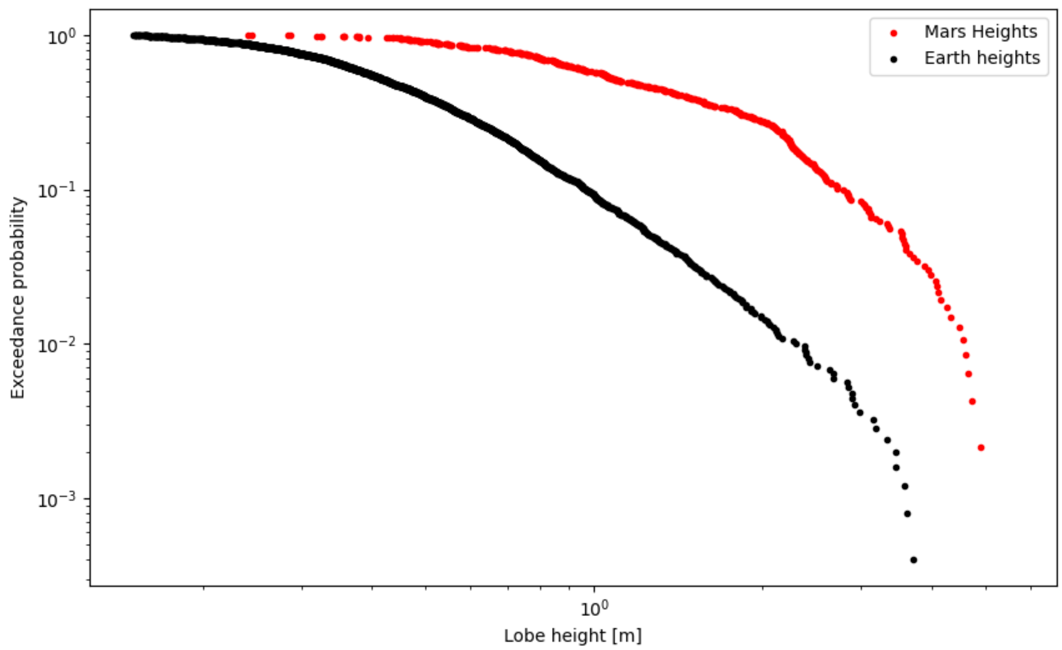


Figure 4: Exceedance probability plot in log log space of lobe height

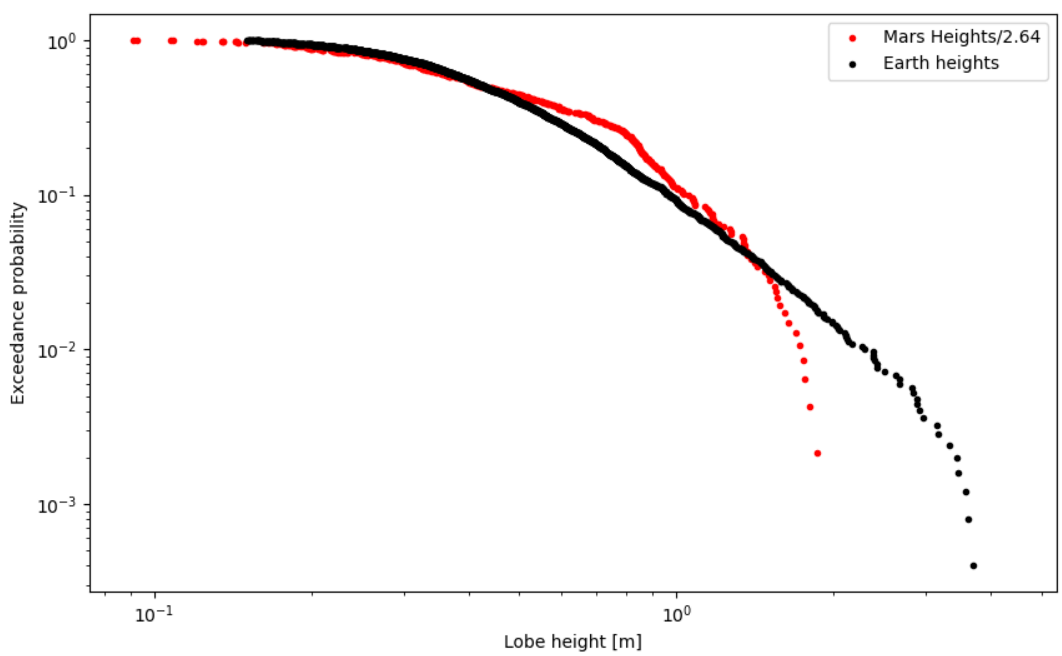


Figure 5: Exceedance probability plot of lobe height in log log space, where Mars heights are divided by 2.64 based on the expected difference in height from Eqn. 2

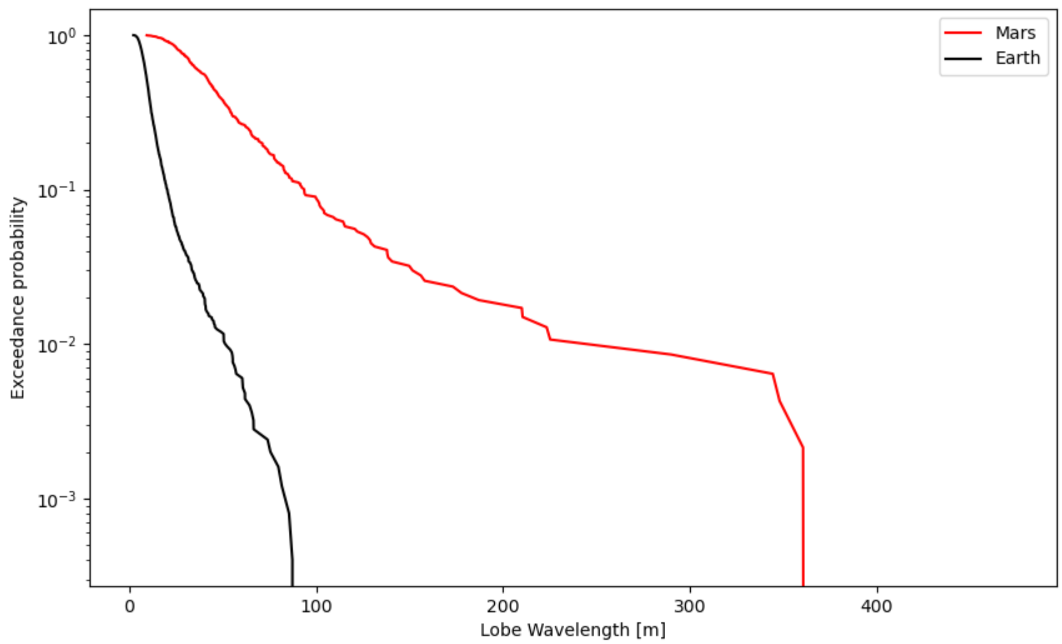


Figure 6: Exceedance probability plot in semi log space of lobe wavelength

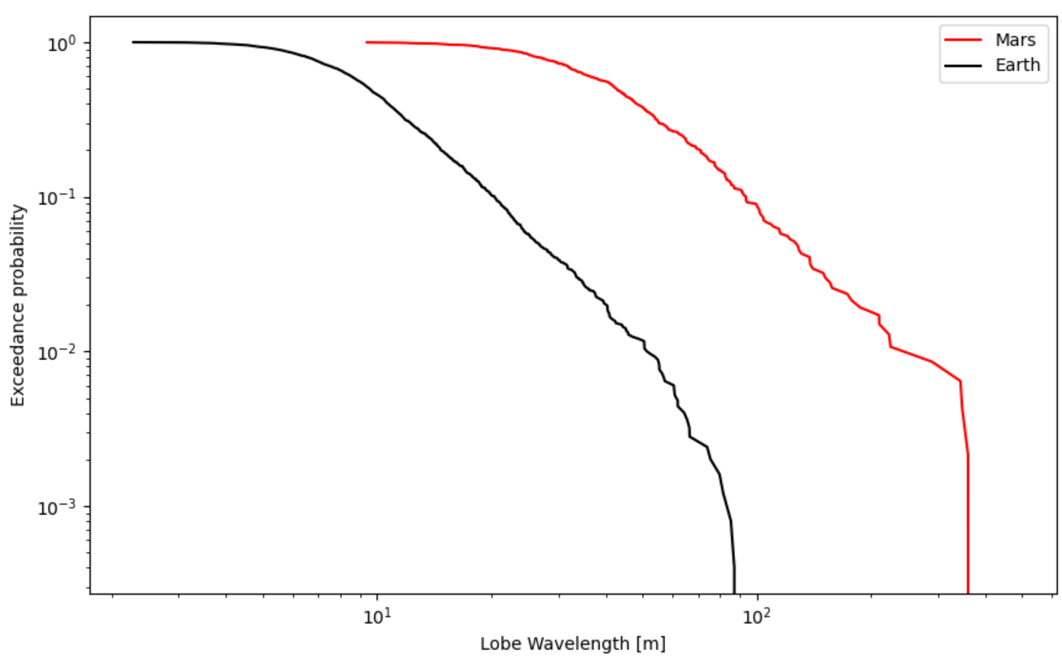


Figure 7: Exceedance probability plot in log log space of lobe wavelength

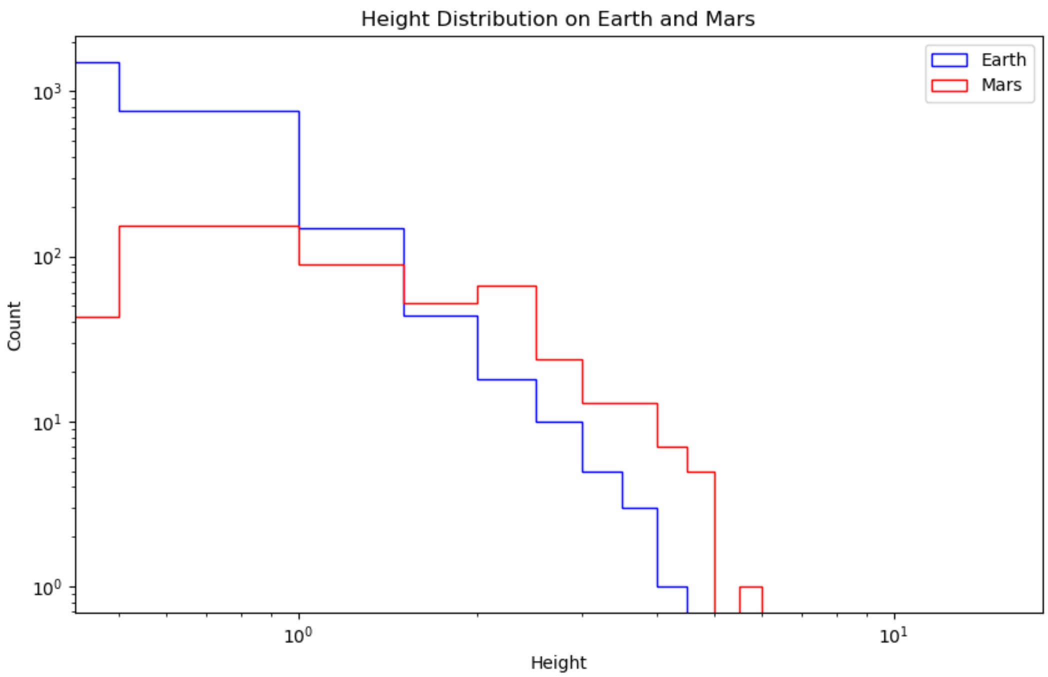


Figure 8: Histogram of lobe heights

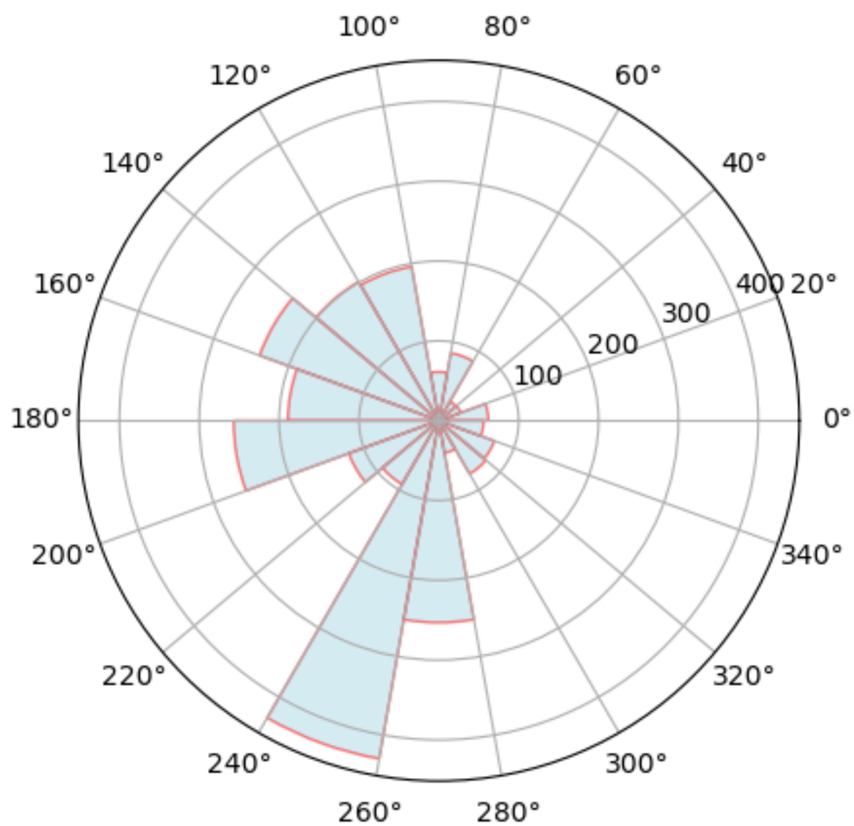


Figure 9: Histogram of lobe aspect for Earth, illustrating difference that these lobes are south west facing compared to the north-west facing Mars lobes

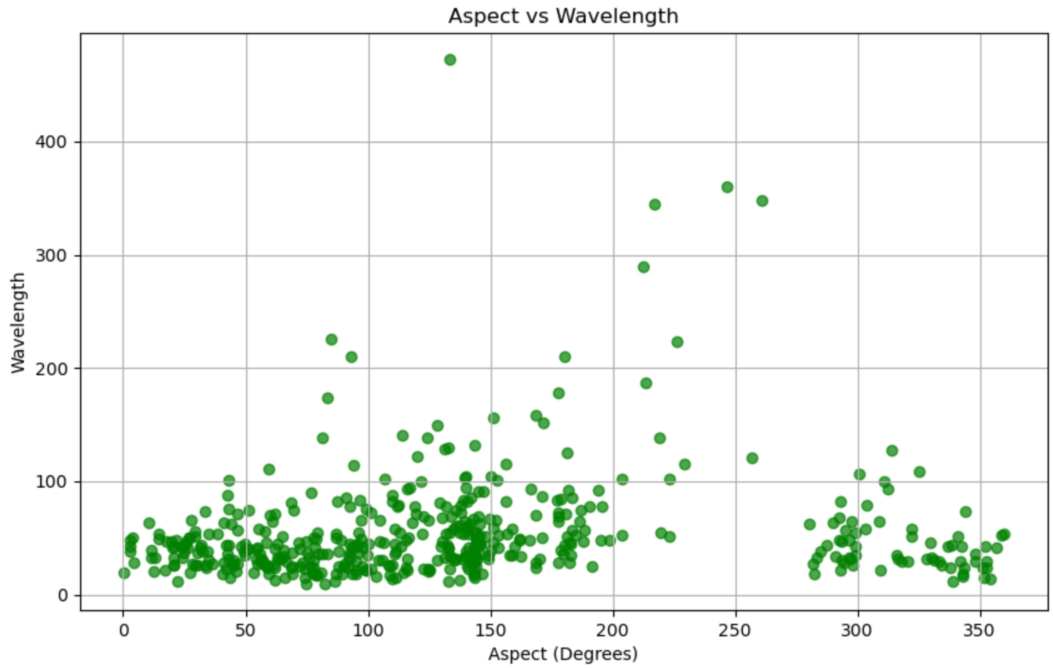


Figure 10: Aspect vs Wavlength for the Mars data points

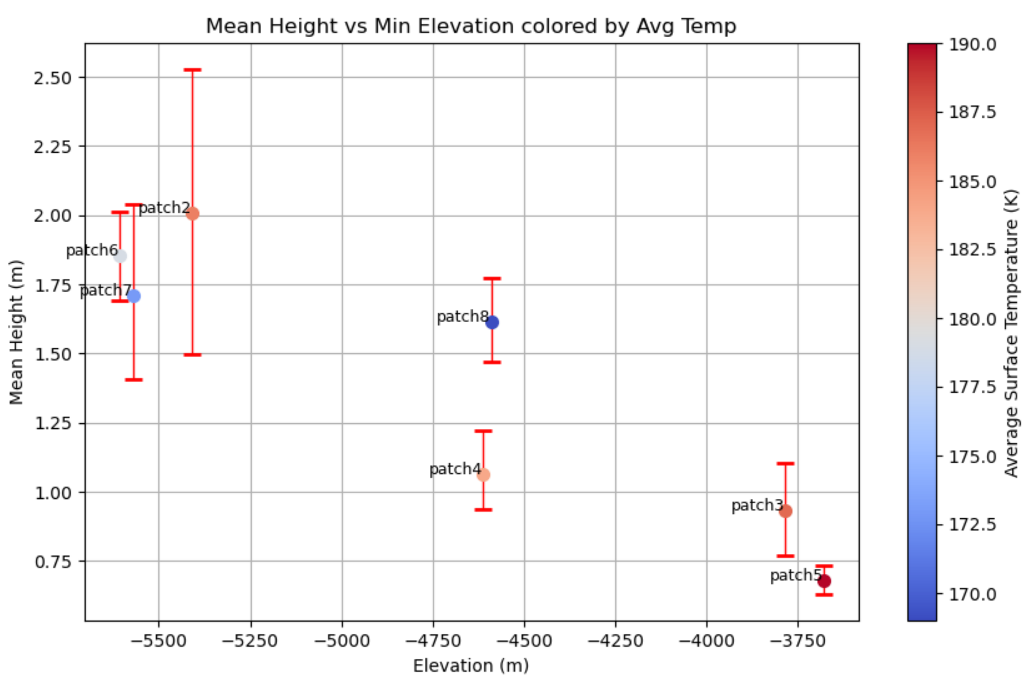


Figure 11: Mean lobe height for each crater plotted against elevation, with points colored Avg temp (Piqueux et al., 2023).

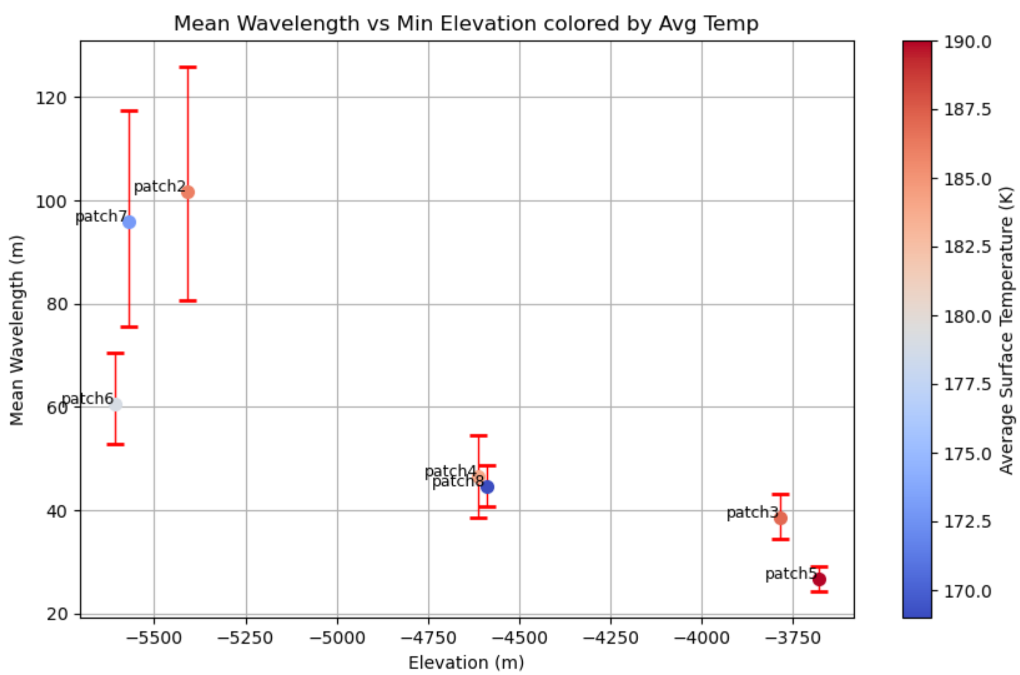


Figure 12: Mean lobe wavelength for each crater plotted against elevation, with points colored Avg temp (Piqueux et al., 2023).

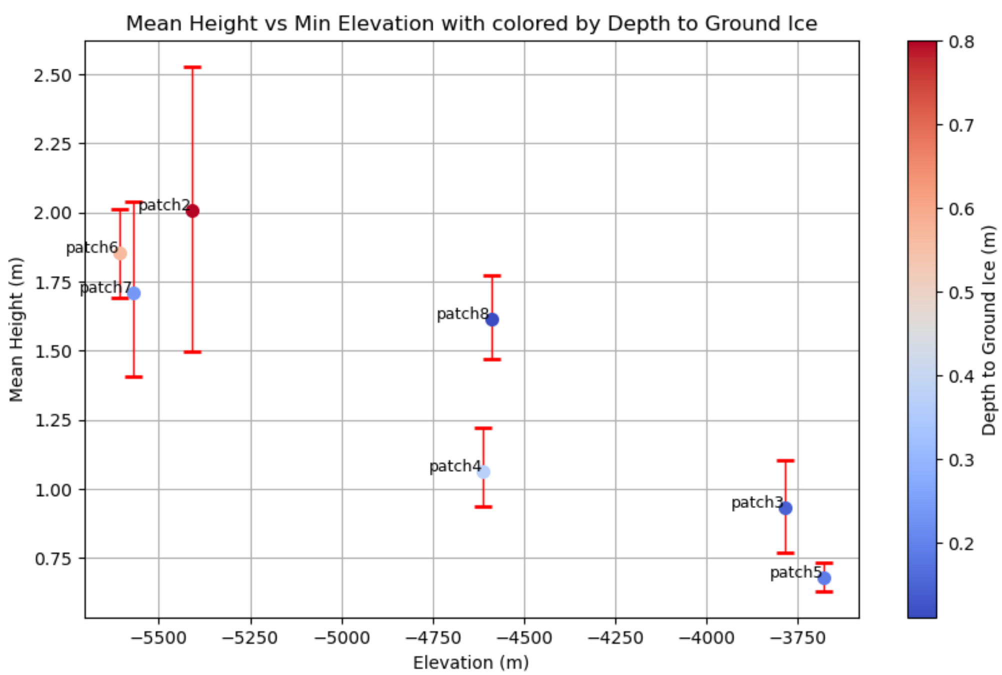


Figure 13: Mean lobe height for each crater plotted against elevation, with points colored by depth to ground ice (Piqueux et al., 2019).

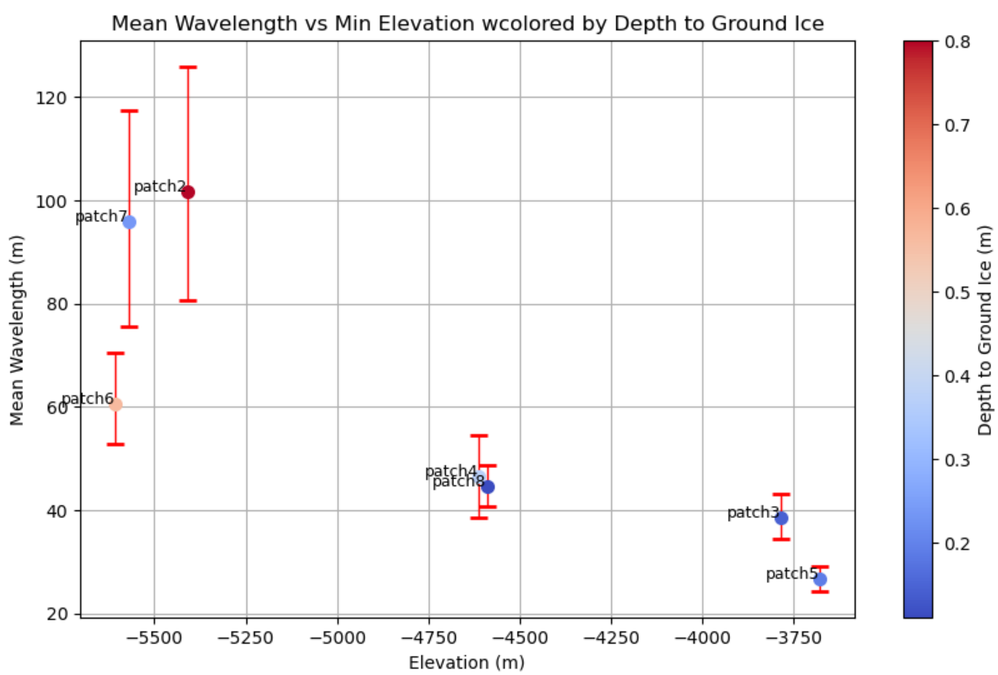


Figure 14: Mean lobe wavelength for each crater plotted against elevation, with points colored by depth to ground ice (Piqueux et al., 2019).

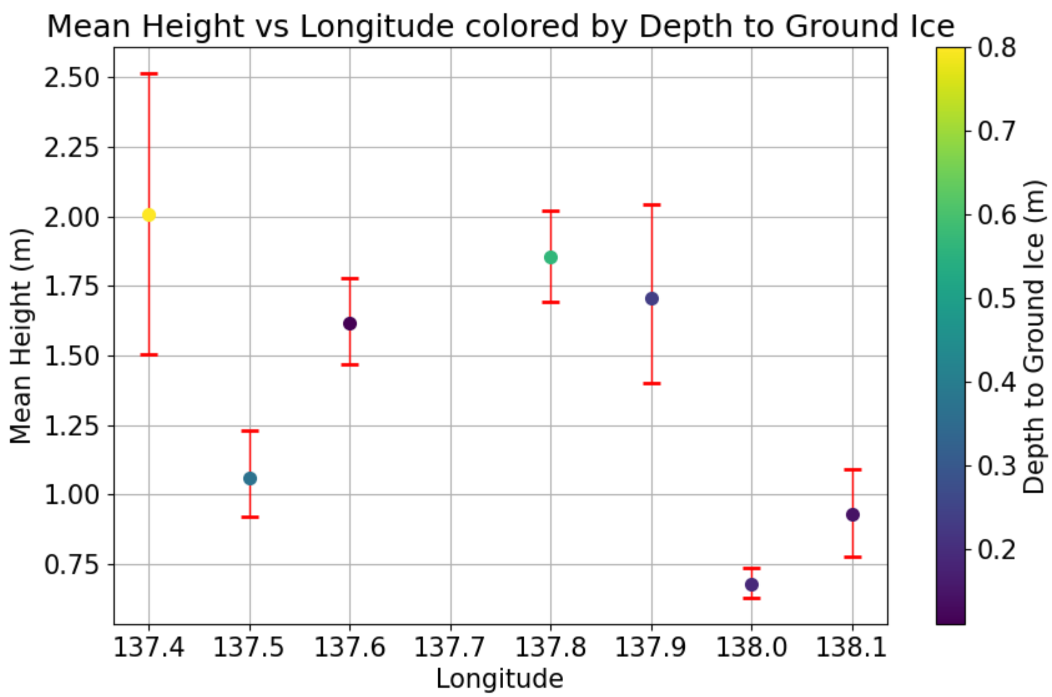


Figure 15: Mean lobe height for each crater plotted against longitude, with points colored by depth to ground ice (Piqueux et al., 2019), showing no correlation.

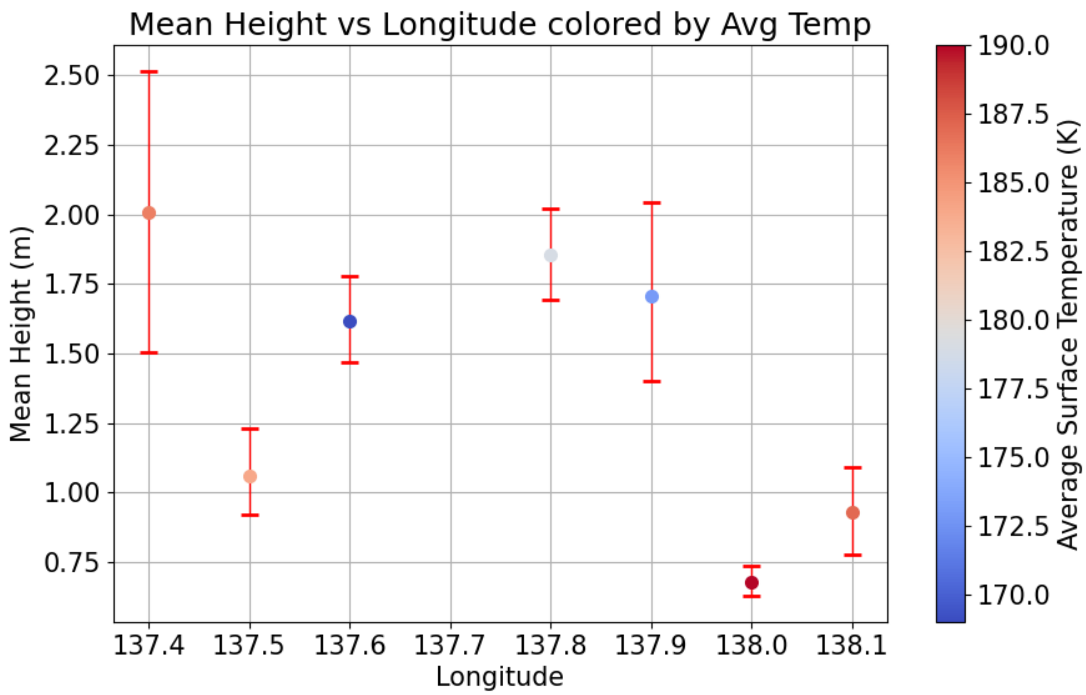


Figure 16: Mean lobe height for each crater plotted against longitude,with points colored Avg temp (Piqueux et al., 2023).

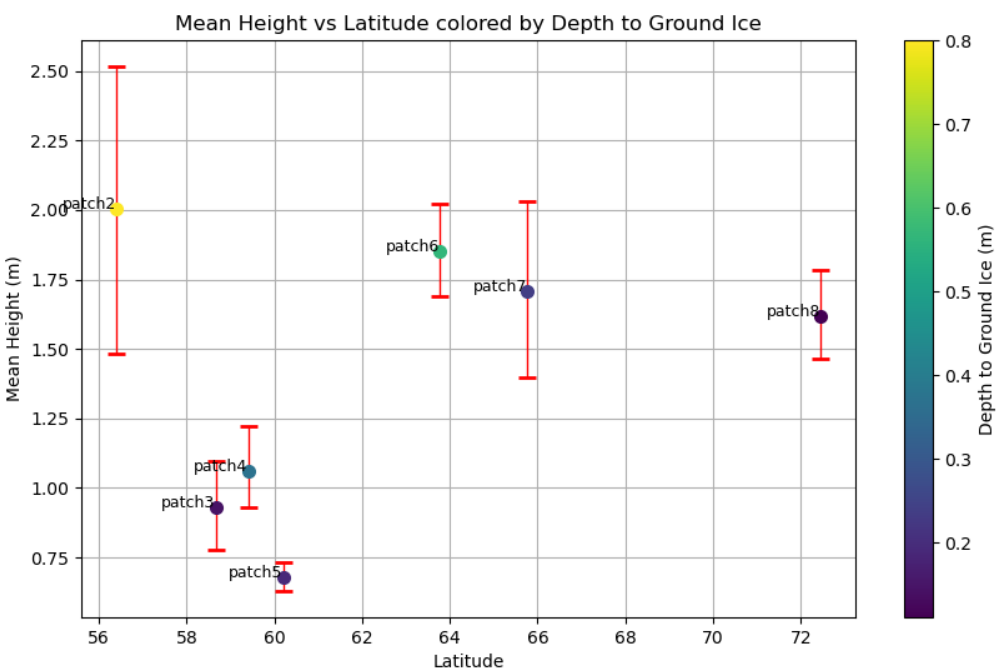


Figure 17: Mean lobe height for each crater plotted against latitude, with points colored by depth to ground ice (Piqueux et al., 2019), showing no correlation.

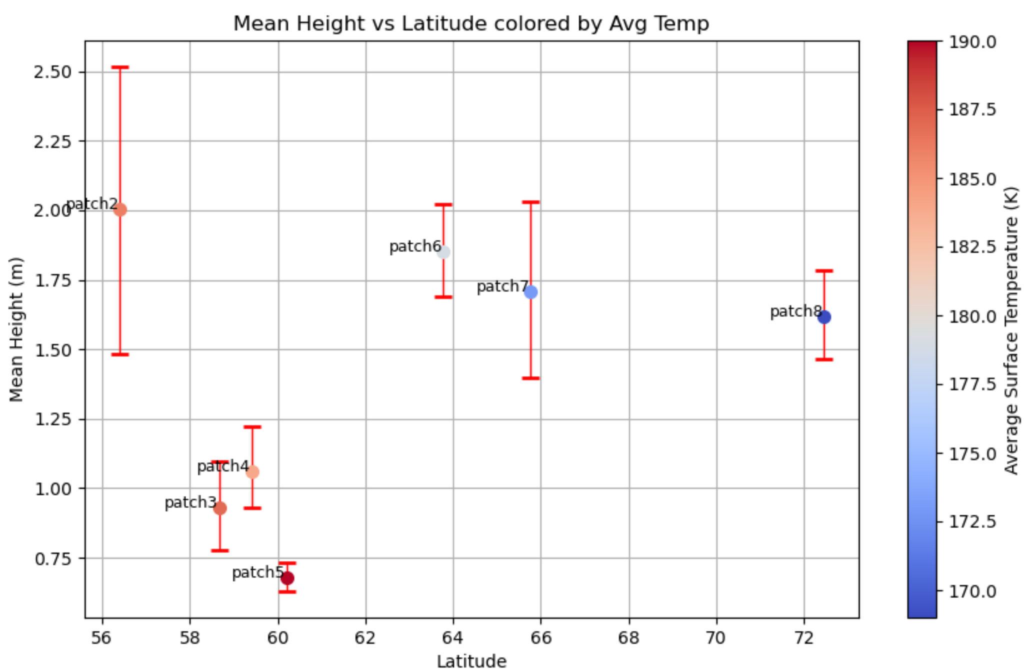


Figure 18: Mean lobe height for each crater plotted against latitude,with points colored Avg temp (Piqueux et al., 2023).